applied mechanics

MDPI

Article

A Novel Meso-Scale Krouse Specimen for Bending Fatigue Characterization: Design Optimization and Experimental Validation

Md Bahar Uddin [1], Tyler Patterson [2], Sriram Praneeth Isanaka [1], Mohammad Masud Parvez [3] and Frank Liou [1,*]

[1] Department of Mechanical and Aerospace Engineering, Missouri University of Science and Technology, Rolla, MO 65409, USA; mbgrm@mst.edu (M.B.U.); sihyd@mst.edu (S.P.I.)
[2] Department of Electrical and Computer Engineering, Missouri University of Science and Technology, Rolla, MO 65409, USA; tkpnm6@mst.edu
[3] Articure Inc., 7555 Innovation Way, Mason, OH 45040, USA; mparvez@articure.com
* Correspondence: liou@mst.edu

Abstract

Miniaturized tests can offer significant material and time savings while still providing representative results comparable to macro-scale tests for relevant applications. Moreover, in challenging fields like hazardous materials research in nuclear, chemical, and similar industries, miniaturized testing presents an even more compelling and practical solution to counter safety, specimen preparation, and material disposal constraints. With an emphasis on optimization to guarantee maximum stress concentration, a uniform stress distribution, and the fact that failure always occurs within the gage, this study investigates the bending fatigue behavior of meso-scale Krouse specimens. Initially, theoretical and finite element analyses were performed for geometry optimization. Subsequently, the optimized geometry was experimentally validated through constant amplitude, load-controlled bending fatigue tests with prescribed stress ratio, $R = 0$. Both theoretical framework and experimental validation confirmed the effective optimization of the specimen design for stress behavior. Furthermore, the S-N curve generated from the experiments demonstrated consistent patterns when compared with analytical and literature data, proving the validity of the optimized specimen design. The scientifically validated specimen design serves as a novel and innovative approach that could be applied in applications where small size, and bending loads are critical.

Keywords: bending fatigue; meso-scale; Krouse-specimen; repeated loading; constant amplitude loading

Check for updates

Received: 21 July 2026
Revised: 21 September 2026
Accepted: 21 September 2026
Published: 23 September 2026

Copyright: © 2026 by the authors. Licensee MDPI, Basel, Switzerland. This article is an open access article distributed under the terms and conditions of the Creative Commons Attribution (CC BY) license.

1. Introduction

The phenomenon of fatigue failure under cyclic loading has been known and studied since the nineteenth century following the Paris railway accident. Subsequently, the fatigue of numerous engineering structures and components, including bridges, automobiles, aircrafts, and nuclear systems has been a major concern among researchers. The stress–life (S-N) approach developed by Wohler with extensive investigations and laboratory testing provided a fundamental framework for characterizing fatigue strength and cycles to failure [1,2]. Since then, a great deal of scientific research and development has been carried out to investigate the fatigue failure mechanism [3–5] and establish testing procedures and

standards such as axial fatigue testing, bending fatigue testing, rotating bending fatigue test, most popularly known as R.R Moore bending fatigue testing, cantilever bending fatigue test, and so on [6–11]. In the current study, the cantilever bending fatigue test procedure is applied following the ASTM standard B593-21 [9].

Miniaturization has popped up in the analytical world with vast applications in not only material characterization, but also in manufacturing, industrial and environmental research with a view to curtailing processing cost, time, and manufacturing complexities [12,13]. But miniature specimens come with their own challenges, and the appropriateness and effectiveness of the miniaturization concepts needed to be convincingly justified. L Bergonzi et al. [14] analyzed and compared the miniature specimens compatible with Mach3D fixtures with full size ISO 6892 standard specimens and reported comparable but identical stress–strain behavior, with a maximum deviation of 3.7% in tensile strength, supporting the feasibility of miniaturization. J Džugan et al. [15] demonstrated and proved the excellent trends in determination of the mechanical characteristics of sheet metal between Mini-Tensile (MT), and standard-sized samples. S. Karnati et al. [16] evaluated the economic, manufacturing, and qualitative benefits of meso-scale specimens relative to existing ASTM E8 geometries, with comparable pre-yield stress–strain behavior, proving the feasibility of using them in various characterizations [17].

Besides mini-tensile tests, miniaturization has also been proven to be justifiable in fatigue testing, offering greater relevance in terms of time and cost efficiency. Although the application in this area remains limited, a few studies are noteworthy. Notably, T. Hirose et al. [18] investigated diametral strain-controlled fatigue tests between mini and normative specimens, where the mini specimen showed a higher fatigue strength than that of the normative specimen. Later, J. Sempruch et al. [19] executed the same concept in an ultrasonic high-cycle fatigue testing machine and found equivalent results with that of conventional servo-hydraulic fatigue machine at reduced timeframes which saved on test costs. While all of these works were implemented in axial and rotating bending fatigue conditions, H. Ghadimi et al. [20] and D. Yang et al. [21] further executed this high-frequency fatigue-test concept in a pure bending fatigue test by using a flat thin specimen instead of a round stock. This allowed us to leverage the cost-effectiveness [22,23] and rapidness of the fatigue test as well as study geometric sensitivity with the help of theoretical analysis, numerical simulation, experimentation, and ML-based prediction [24–27].

As miniaturization becomes prevalent, some past investigations have argued that size can affect fatigue strength if there is a stress gradient prominent in the specimen due to certain unusual geometric features such as holes, notch, fillets, etc., and can be amplified by variances in surface finish [28,29]. Intrinsically, the presence of peculiar geometric patterns, although unavoidable in the practical world, causes unwanted stress-concentration zones, leading to the perceived reduction in the material strength [30]. C. Sun et al. [31] also identified some of the benefits of the notched geometry which provides a contrarian perspective on the use of these geometric features. In their analysis, they reasoned that the specimen having notched features exhibits higher fatigue strength due to its smaller control volume than a normal specimen, resulting in fewer inclusions or defects that would adversely affect fatigue behavior. However, such an effect can be specific to aspects such as different materials exhibiting differing sensitivity to size in determining fatigue properties [32–34]; specimen shape and design variables that could dominate fatigue strength [35,36]; surface condition, where poor finishes from manufacturing process as well as the test procedures significantly affect the fatigue performance [37,38].

With respect to geometry, the Krouse shape has recently appeared as a leading choice in bending fatigue tests due to its consistency of stress distribution across the gage area by reducing stress concentration points and thereby providing reliable data on material

properties. Additionally, recent research has highlighted the benefits of this method for metal characterization, especially in bending fatigue tests on flat sheets, as it allows for the analysis of a larger volume of material compared to gage sections of uniform cross-section. M.M Parvez et al. [39,40] used a dual gage Krouse specimen in their fatigue test of additively manufactured material, as it provides a larger surface area to increase control volume, which would enable higher volumes of surface and microstructural defects to be captured, interrogated, and analyzed, thereby generating representative data. Krouse-type fatigue differs when compared to axial fatigue testing, requiring less force to achieve the same stress amplitudes and using less expensive testing machines as demonstrated by Z. R Williams [41]. Researchers have also demonstrated the application of Krouse specimen in their respective analyses at multiple size scales [42–46]. Gohil et al. [47], Berchem et al. [48] and Haidyrah et al. [49] experimented with Krouse specimen in sheet metal and nuclear materials, respectively, to determine bending fatigue properties with the application of the stress-life (S-N) approach.

All the studies described above have demonstrated the feasibility of specimen miniaturization and the application of Krouse geometries at different scales. However, limited attention has been given to systematic design optimization and validation of a meso-scale Krouse geometry for bending fatigue characterization. To address this gap, this research attempts to develop a holistic strategy for Krouse-type geometry development by further scaling down the test specimen size into the meso-scale regime [50], while minimizing manufacturing constraints and unintended stress concentrations. Meso-scale was chosen as it can yield an optimal balance between resource efficiency and data representativeness. The optimization process includes theoretical analysis and finite element simulation, followed by experimental validation under constant amplitude loading at the prescribed stress ratio of $R = 0$. The novelty of this work lies in integrating specimen miniaturization, achieving a nearly uniform stress distribution across the gage section, and promoting failure within the gage sections. The resulting approach is intended to save material, specimen-preparation time, and testing requirements while retaining representative fatigue behavior, thereby providing a viable basis for bending fatigue characterization where material availability, cost, or specimen size is constrained.

2. Materials, Assumptions and Methodology

2.1. Materials

The material analyzed as an example to support the current study was 17-4 PH, which is a stainless steel that finds broad applicability in aerospace, plastic molding dies, and chemical processing components due to its remarkable corrosion-resistant property [51]. It is a precipitation hardened SS comprising approximately 17% chromium and 4% nickel, providing an outstanding combination of high strength, and hardness as well as a surface finish that is not affected by significant oxidation effects. The chemical composition of the steel received through Mill Test Certificate (MTC) from the vendor is listed in Table 1. The commercially purchased steel was in the solution annealed (condition A) state, allowing for easy machinability with a 34 HRC and grain size finer than 10.5, that would theoretically lead to improved fatigue resistance and performance characteristics [51,52].

Table 1. Chemical composition of 17-4 PH steel.

Element	C	Mn	P	S	CB	Si	Cu	Ni	Cr	Mo	Ta	Co
Wt. %	0.04	0.52	0.022	0.0001	0.29	0.24	3.27	4.78	15.37	0.2	0.01	0.06

2.2. Assumptions

Despite the extensive initiatives taken during the analysis to acquire consistent results; this analysis makes some typical assumptions as described below which help to simplify the interpretation and calculation throughout the testing and experimentation.

- The material used in this test is homogeneous and isotropic in terms of composition and properties.
- The material follows Hooke's law within the elastic range.
- In spite of polishing to achieve a high surface finish, surface defects such as scratches, voids, oxides might exist in a minimal amount which have negligible effects that are beyond the scope of this study.
- The load applied in a test cycle is uniform and constant.
- The experimental test setup has been designed and manufactured for a bending fatigue test, and any internal shear, torsional, or axial load is considered negligible.
- The residual stress effect in material from prior manufacturing is not considered.
- Due to geometric variations in portions of the specimen, the calculated stress concentration is assumed to be approximate.
- The tolerance in dimensions and thickness of the specimen is within 2%.
- Specimen is treated as a cantilever beam and follows the elastic-static theory also known as the Euler–Bernoulli hypothesis [53] which states that plane sections of the beam remain in plane after bending and cross section remains normal to the neutral axis.
- The frictional effect between moving components in practical test setup is negligible.
- The test is performed at room temperature, which is assumed to remain constant throughout the test at a frequency of 10 Hz.

2.3. Methodology

2.3.1. Preliminary Specimen Geometry

Preliminary specimen geometry, a modified version of ASTM suggested standard for Krouse-type bending fatigue [9] was created by using SolidWorks 2023 (Dassault Systèmes-SolidWorks Corporation, Vélizy-Villacoublay, France) as indicated in Figure 1. The overall dimensions and volume were estimated to be one-fourth of the closest comparable ASTM bending-type specimen, which categorizes this design into the meso-scale specimen regime [50]. Additionally, the holes present in ASTM geometry for clamping and loading have been avoided to eliminate undesirable stress concentration at those highly notch-sensitive features as well as to simplify the specimen manufacturing and preparation process. Inclusion of these features adds additional manufacturing operations and introduces tolerance and surface finish complexities particularly in miniaturized designs, which this research wishes to counter.

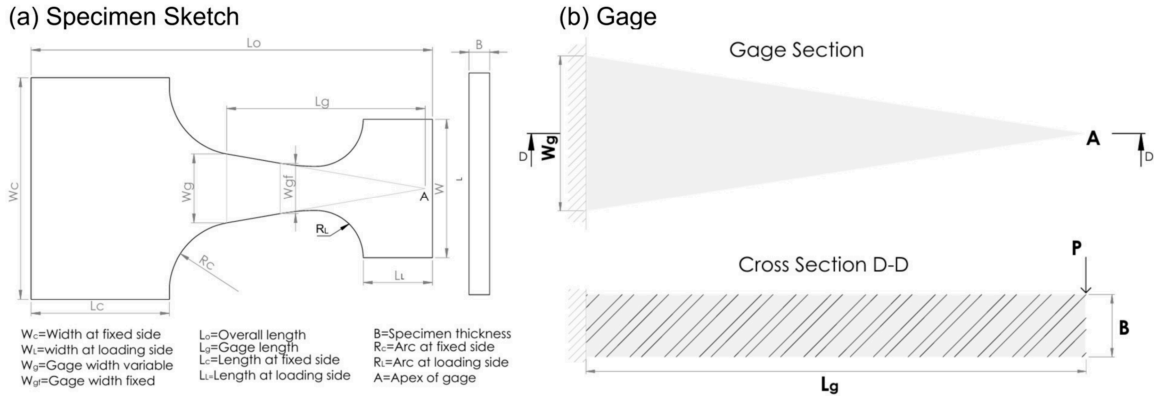


Figure 1. Preliminary specimen design; (**a**) Specimen sketch, (**b**) Gage.

The geometric parameters shown here have been optimized through iterative refinement using FEA simulations. Specifically, the arc (R_c) and clamping area have been configured for providing sufficient reinforcement against reaction forces, hence alleviating the stress concentration in the clamped section and to transfer and locate the maximum stress concentration regions to the gage. With W_{gf} approximated to a certain value, W_g (the gage width) is the controlling variable for optimizing the gage region, such that changing W_g automatically adjusts the gage length and Apex A (the loading point).

2.3.2. Theoretical Study

In the design optimization process of fatigue specimens, a theoretical study is essential to reduce excessive empirical iterations and the need for superfluous physical prototyping. Theoretical calculations leveraged by this study provided preliminary benchmarks to carry the analysis forward through simulated data and supporting empirical evidence. This also provides other researchers with the methodology to create and optimize their own miniature Krouse-type geometries to address their own unique needs.

2.3.3. Stress and Deflection Calculation

The theoretical analysis of this study focuses on the gage section, considering it as a cantilever beam which is fixed at one end and deflects at the other end when subjected to a load P as shown in Figure 1b.

In this case, per ASTM, the simple beam equation can be used to calculate maximum bending stress [9]. Additionally, several other researchers have derived the forthcoming equations for maximum bending stress and deflection, incorporating the local section property and bending moment of a triangular beam [44,47,48,54].

$$\sigma_{\max} = \frac{6\, L_g\, P}{W_g\, B^2} \tag{1}$$

$$\delta = \frac{6\, P\, L_g^3}{E\, W_g\, B^3} \tag{2}$$

where σ and δ, P, L_g, W_g, W_g and E are maximum stress, deflection, load, gage length, gage width, specimen thickness and modulus of elasticity of the material, respectively. These notations are mentioned according to ASTM standard terminology relating to fatigue and fracture testing from the "E1823-23" standard document [55].

Even though proper care has been taken in specimen design to avoid certain features, due to the nonuniform gage section of Krouse geometry, there will still be an effect of the geometric stress concentration factor. Moreover, regardless of 17-4 PH steel being ductile, in fatigue testing to high cycles with the application of cyclic loading, dynamic stress concentration exists due to notch sensitivity at filleted sections. Neuber and Kuhn established the following relationship between this geometric stress concentration K_t, notch sensitivity, q and fatigue stress concentration K_f [1,56,57].

$$K_f = 1 + q(K_t - 1) \tag{3}$$

Geometric stress-concentration data compiled by numerous experts are available in the literature in the form of charts and tables for basic geometric shapes such as stepped flat bar, grooved shafts, notched and filleted rectangular bars, etc., [58–60]. For more complex shapes, the mathematical function as shown in Equation (4) plus a list of coefficients is suggested in Pikey–Peterson's stress concentration factor, and *Machine Design: An Integrated*

approach [1] and is assumed to be the closest match for analyzing stress concentration in the current Krouse design.

$$K_t = A\left(\frac{r}{d}\right)^b \tag{4}$$

where K_t is calculated by measuring the major (D) and minor (d) width (W_c and W_g in Figure 1) in the respective fillet (r) throughout the Krouse cross-section. The coefficients A and b are obtained through interpolation based on the data available in the literature.

Material notch sensitivity, q is defined in terms of Neuber's constant, and notch (fillet in this case) radius is stated in Equation (5) through the Kuhn–Hardrath formula [1,56].

$$q = \frac{1}{1 + \sqrt{\frac{a}{r}}} \tag{5}$$

The Neuber's constant, $\sqrt{a}$ can be determined from the ultimate strength of the material using the charts available in the literature [1,61]. By substituting K_t and q values into Equation (3), fatigue stress concentration K_f is determined. Finally, Equation (1) is revised to the following form to calculate the maximum local bending stress.

$$\sigma_{\max} = K_f \frac{6 \cdot L_g \cdot P}{W_g \cdot B^2} \tag{6}$$

Endurance Strength Calculation

Endurance strength refers to the stress level that a material can withstand for an infinite fatigue cycle without experiencing failure. In the context of the S-N curve, endurance limit exhibits the knee point past which a material will experience no failure in its lifetime of repeated load cycling. Generally, the endurance strength of the material is estimated with respect to its ultimate strength [1]. For example, if steel's UTS is less than 1400 MPa, the estimated endurance strength, $S'_e = 0.5S_{ut}$. This estimation is based on standard fatigue-test specimens through static testing. In actual applications, several other factors such as size effect, type of loading, surface finish, environmental impact and, finally, reliability factor must be considered. So, by multiplying all those factors with estimated endurance strength, the corrected endurance strength is obtained using the following equation.

$$S_e = C_{\text{load}}\, C_{\text{size}}\, C_{\text{surf}}\, C_{\text{temp}}\, C_{\text{reliab}}\, S'_e \tag{7}$$

The factors in Equation (7) are calculated by using the formula in the book "*Machine design-An Integrated Approach*" [1] and are described in the forthcoming sections.

C_{load} = loading factor. In a bending fatigue test, loading factor is always 1. So, $C_{\text{load}} = 1$.

C_{size} is the size factor that needs to be considered for larger specimen size where diameter exceeds 8 mm. However, in this study, as we are dealing with meso-scale flat specimen, an approximate equivalent diameter is calculated by using the formula:

$$d_{\text{equiv}} = \sqrt{\frac{A_{95}}{0.0766}} \tag{8}$$

where A_{95} is the cross-sectional area of the specimen stressed above 95% of its maximum stress compared to a rotating beam specimen. By calculating this, d_{equiv} is found to be 2.04 which is less than 8. So, in this current study, $C_{\text{size}} = 1$.

C_{surf} The surface factor data is available in the literature with respect to the ultimate strength of the material but the relationship in Equation (9) has been established by Shigley et al. to determine specific results in actual applications [61].

$$C_{surf} \approx A(S_{ut})^b \tag{9}$$

In the current study, surface factor is calculated as C_{surf} = 0.69, using Equation (9) by selecting the coefficient A and exponent b from table available in Shigley and Mischke, *Mechanical Engineering Design*, 5th ed., McGraw-Hill, New York, 189, p. 283 for machined specimen [62].

C_{temp} The temperature factor is 1 for this case as the test is performed at room temperature.

Finally, assuming 99% reliability on used material strength, C_{reliab} = 0.814. The corrected endurance strength S_e derived from Equation (7) is then used as a knee point in the S-N curve.

Theoretical Life Cycle Calculation

To create an estimated S-N curve, theoretical life cycle is calculated by using Equation (10).

$$S(N) = aN^b \tag{10}$$

where $S(N)$ is fatigue strength at any cycle N; a, b are the fatigue life-cycle constant, and fatigue strength exponent, respectively, determined by the boundary conditions considering fatigue strength, $S(N) = S_m$ at low cycle, $N_1 = 10^3$ while $S(N) = S_e$, at high cycle, $N_2 = 10^6$. Low cycle fatigue strength for bending is estimated as a fraction of ultimate stress and defined as S_m = 0.89 S_{ut} [62,63]. Logarithmic form of Equation (10) is

$$logS(N) = loga + blogN \tag{11}$$

$$b = \frac{1}{z} log\left(\frac{S_m}{S_e}\right) \tag{12}$$

$$z = logN_1 - logN_2 \tag{13}$$

Equivalent Reversible Stress

The current analysis is based on repeated loading with the prescribed stress ratio of $R = 0$; however, the typical S-N curve is only applicable for completely reversible loading ($R = -1$) with zero mean stress effect. Therefore, an equivalent reversible stress must be determined due to the presence of combined mean and alternating stress effect during this fatigue failure. Modified Goodman correction was considered in this analysis, which is demonstrated by Equation (14), where σ_a and σ_m are alternating and mean stress components, while S_e and S_{ut} are the endurance strength and ultimate strength respectively.

$$\sigma_a = S_e\left(1 - \frac{\sigma_m}{S_{ut}}\right) \tag{14}$$

Figure 2 shows that the modified Goodman line is created by linking ultimate strength at abscissa (σ_m) and endurance strength at ordinate (σ_a) as suggested in the modified Goodman diagram. Consequently, the extended line connecting $(S_{ut}, 0)$ and multiple fluctuating stress points (σ_m, σ_a) towards ordinate represents the equivalent reversible stress (σ_{rev}). This is because the point where it intersects at σ_a axis has zero mean stress ($\sigma_m = 0$) which meets the requirement of traditional S-N curve. Accordingly, Equations (10) and (14) are modified, replacing S_e or $S(N)$ by σ_{rev} to calculate respective equivalent reversible stress components and life cycles which are used in creating the S-N curve. σ_a

and σ_m are calculated applying actual fatigue stress concentration factor K_f. Additionally, the mean fatigue stress concentration factor K_{fm} = 1 is considered in the situation of local yielding where maximum stress exceeds the yield strength ($\sigma_{max} > Sy$) [62].

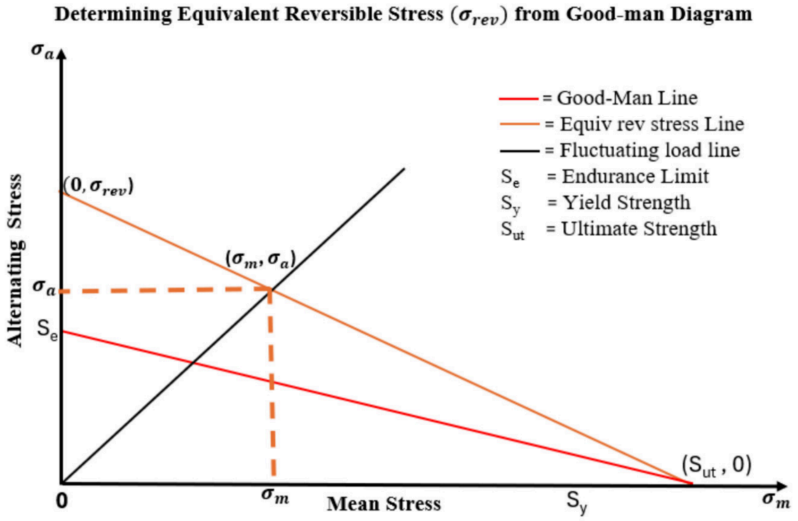


Figure 2. Determination of equivalent reversible stress using modified Goodman diagram.

3. Geometry Optimization and Design Finalization

3.1. FEA Model Setup and Boundary Conditions

The FEA model for the specimen was set up for homogeneous, isotropic, linear-elastic material using the mechanical properties of 17-4 PH steel. The clamped end of the specimen was fully constrained by restricting all translational and rotational degrees of freedom, representing the rigid clamping condition of the cantilever-bending fixture, and eliminating stress concentration from the constrained section. Transverse shear exists in a limited amount, which was considered negligible compared to the bending response across the gage.

A curvature-based blended mesh consisting of solid tetrahedral elements was employed for all geometries. The final mesh contained approximately 61,504 elements and 93,178 nodes, with a characteristic element size of 0.187735 mm. Mesh convergence was evaluated by progressively refining the mesh and monitoring the resulting maximum stress. The final mesh was selected when the variation in the calculated stress between successive refinements remained below 2%, indicating adequate mesh independence for the comparative geometry analysis.

A 15N constant load was applied for the geometry-optimization analyses. The loading location was defined according to the position of the triangle apex associated with each individual gage geometry so that the effective loading condition remains geometrically consistent as the gage width was varied. Additional analyses at higher and lower load levels were also performed to verify that the observed stress-distribution pattern and the relative location of maximum stress were not specific to the selected 15 N load. Under these consistent boundaries, loading, and meshing conditions, the effect of varying gage geometry on the magnitude and location of the maximum stress could therefore be directly compared.

3.2. Geometry Optimization Using FEA

A parametric FEA study was conducted on four separate geometries of the specimen for the optimization and to illustrate the stress propagation within the gage section by using SOLIDWORKS 2023 software (Dassault Systèmes-SolidWorks Corporation). As the core focus is to maximize the gage region (and thereby the effective interrogation volume of the material being tested), other geometric features like the larger width of the gage

trapezoid have been configured and fixed by optimization through these simulations. The gage widths 2.0 mm, 2.5 mm, 3.0 mm, and 3.5 mm were analyzed to observe uniformity or lack thereof of the stress evolution within the gage volume. Figure 3 represents all four geometries along with the respective demonstration of stress distribution.

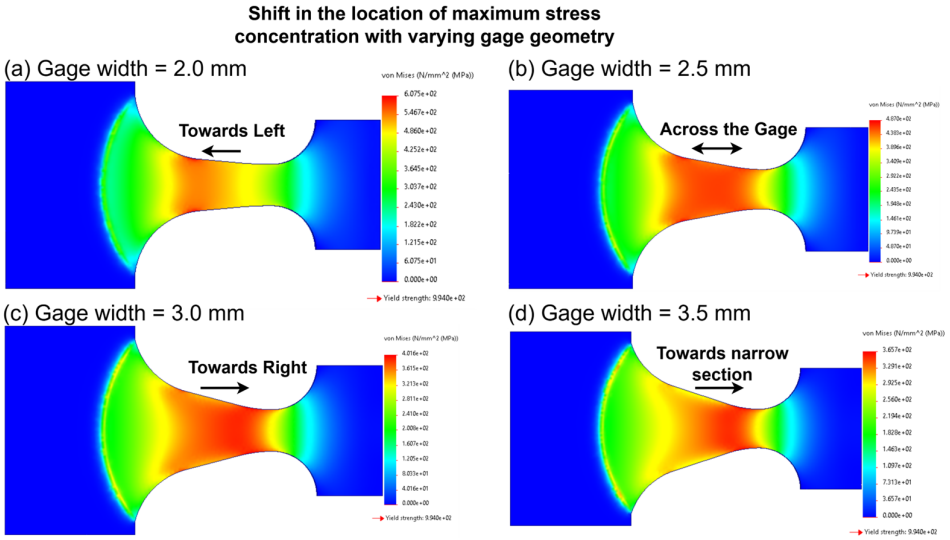


Figure 3. Effect of gage width on the maximum stress distribution within the gage section.

Looking at four distinct demonstrations, the 2.5 mm gage exhibits more balanced distribution than the other three geometries. The 2.0 mm width tends to shift stress concentration towards the clamping side and concentrates the maximum stress concentration to a smaller cross section, while the 3.5 mm width shows a tendency to concentrate towards the loading end. This will tend to initiate and propagate fatigue failure within much narrower regions of the gage while exhibiting non-uniformity in stress distribution across the gage.

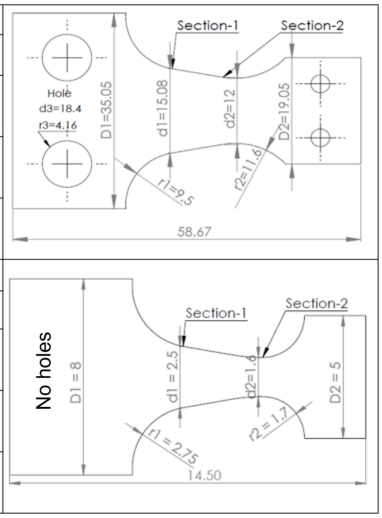
So, it can be stated that lowering or increasing the width beyond a point does not support gage volume maximization, but it raises the risk of failure always occurring at a narrow location, which goes against this research's desire to maximize the gage volume.

3.3. Numerical Validation of Optimized Geometry

Both theoretical and numerical investigations suggested that geometry containing 2.5 mm gage width (Figure 3b) can be utilized as an optimized Krouse fatigue specimen for further investigations.

The optimized geometry is expected to outperform existing ASTM fatigue specimens in multiple ways. One of the standout advantages of this optimized geometry is that it has significantly removed stress concentration, and notch effect by maximizing gage volume, appropriately reinforcing the notches and hence uniformly distributing stress concentration throughout the gage. To validate this statement, stress concentrations in gradually varying cross-sections of the optimized geometry were determined by utilizing relevant equations and we subsequently compared the stress concentration and notch effects of the optimized geometry with ASTM design as presented in Figure 4. It shows that optimized geometry completely eliminated the stress concentration of holes by removing these features and additionally, the stress concentration in the filleted section has been reduced by approximately 20% compared to ASTM design.

Sections	ASTM		
	K_t	q	K_f
Fillet section-1	1.07	0.99	1.07
Fillet section-2	0.96	0.99	0.96
Holes	1.45	0.99	1.45
Sections	**Optimized Geometry**		
	K_t	q	K_f
Fillet section-1	0.88	0.98	0.88
Fillet section-2	0.89	0.98	0.89
Holes	-	-	-



Kt = Geometric stress concentration factor; q = Notch Sensitivity, K_f= Fatigue stress concentration factor

Figure 4. Comparison of stress-concentration between optimized geometry and ASTM design across gradually varying cross-sections and holes (unit = mm).

To verify the effectiveness of the selected geometry, its peak stress maps were compared with those of other geometries assessed in this study by finite element simulations as illustrated in Figure 5. Under identical loading and boundary conditions, even a slight variation in geometry in the gage length and width considerably affected the maximum stress propagation.

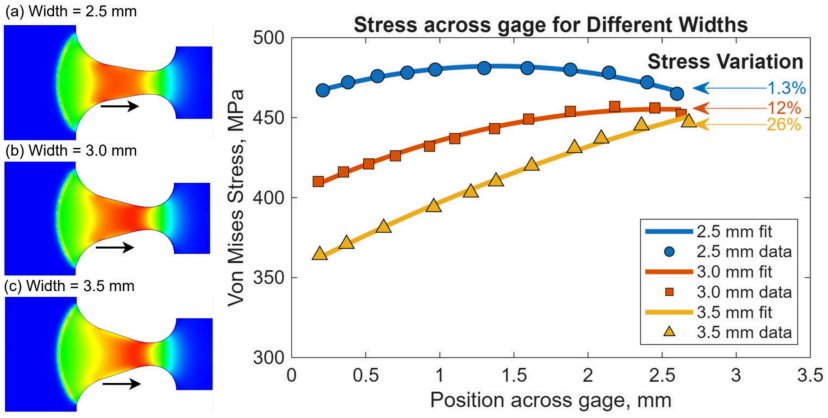


Figure 5. Variation in stress gradient across the gage in different geometries (based on FEA data).

The Von Mises stress was recorded along a consistent path extending from one end of the gage to the other, as indicated by the arrows in Figure 5a–c. The percentage stress variation was determined from the stress variation between two ends of this path relative to the higher stress value in each geometry. The plot shows that optimized geometry experienced only 1.3% variation in maximum stress, whereas other geometries exhibited 12% and 26% variation among the nodes across the gage, reflecting the effectiveness of the gage optimization and demonstrating the 2.5 mm width as a balanced geometry.

4. Experimental Methodology

4.1. Specimen Preparation

Premised on FEA optimization results, the specimen geometry incorporating a 2.5 mm gage width was selected as the final design, as illustrated in Figure 6. This configuration provided the most uniform stress distribution across the gage section while maximizing the

effective material volume in the gage for fatigue interrogation. The remaining geometric features were retained from the preliminary design, resulting in a specimen that satisfies both the dimensional constraints of the meso-scale test and the mechanical requirements for reliable bending fatigue characterization. The optimized specimens were prepared using a wire-electric discharge machine (W-EDM) from a commercially purchased 17-4 PH stainless steel block. As the machining of miniature specimen is quite challenging in terms of dimensional accuracy and minimizing surface roughness, initially some test cuts were performed to acquire a suitable combination of machining parameters such as pulse, peak current, feed and wire speed, etc., [64]. Moreover, to avoid an oxide layer along the profile, this machining process featured an initial rough cutting pass followed by three finishing passes as suggested by Karnati et al. [16].

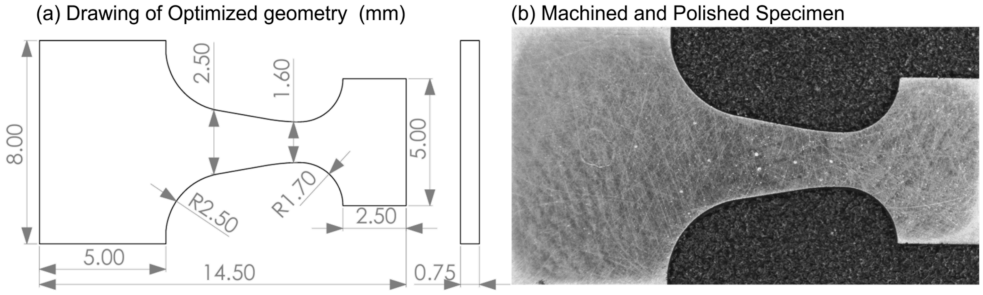


Figure 6. Meso-scale optimized specimen; (**a**) drawing of the optimized geometry, (**b**) machined specimen.

Machined specimens underwent some micro and macro polishing [65,66] to remove any subsequent oxide layers and surface imperfections while maintaining dimensional tolerances. These manual polishing processes were performed in two sequential stages; primarily, 400 and 600 grit emery paper was applied to remove the oxide buildup, detrimental burrs, and tooling scratches. Subsequently, 800, and 1200 grit sandpaper were deployed to ensure a smoother surface finish with minimal stress concentration points. Final specimen dimensions, including thickness and surface roughness, were reported in Appendix A, Table A1. Despite the polishing process, minor surface irregularities and polishing marks remained; therefore, the machined-surface correction factors were adopted as presented in Table 2, and discussed in the Section: Endurance Strength Calculation. Additionally, the potential influence of surface roughness, dimensional tolerances, wire EDM-induced surface characteristics, and effect of residual stress on fatigue behavior were not quantified in the current study. The authors have planned for these as scope of future studies.

Table 2. (**a**) Mechanical properties of 17-4 PH steel from tensile test (measured), (**b**) endurance strength correction factor (calculated), (**c**) fatigue strength properties (calculated).

(a) Mechanical Properties of 17-4 PH Steel from Mini- Tensile Test (Measured)					
Properties	(S_{ut}), MPa	YS (0.2%), MPa	E, GPa	Strain at Break mm/mm	
Value	1172	994	205	0.23	
(b) Endurance Strength Correction Factors (Calculated)					
Factors	C_{load}	C_{load}	C_{surf}	C_{temp}	$C_{reliability}$
Value	1	1	0.69	1	0.814
(c) Fatigue Strength Properties (Calculated)					
Parameters	S'_e, MPa	S_e, MPa	a, MPa	b	
Value	585	330.53	3287	−0.1663	

4.2. Test Setup

Figure 7 outlines the schematic presentation of a miniature fatigue test apparatus which was developed for experimental validation of optimized geometry. The set-up comprises some key components such as (i) a voice coil actuator, (ii) a laser displacement sensor, and (iii) specimen mount including clamps, fixtures, and a load cell. The 3-inch diameter linear voice coil actuator possesses the continuous stall force capacity of 133.8 N with maximum allowable coil winding temperature of 155 °C that makes it best fit for the high-cycle fatigue test application. The wider portion of the specimen is secured in a fixed jaw while the loading end is clamped to a movable block which travels along the sliding guide rail and is attached to the actuator. A 25 lb capacity pre-calibrated load cell (FUTEK LCM 100) is mounted right after the moving jaw for accurate measurement of the load applied on the specimen. Prior to mounting, the load-cell calibration was justified using zero and span potentiometer adjustments, with the zero-load output adjusted to approximately 0 VDC and the output under a known reference load adjusted to the corresponding calibrated value of 10 VDC. The zero and span outputs were subsequently reverified before installation. The power is supplied to the motor using a DC310S benchtop power supply.

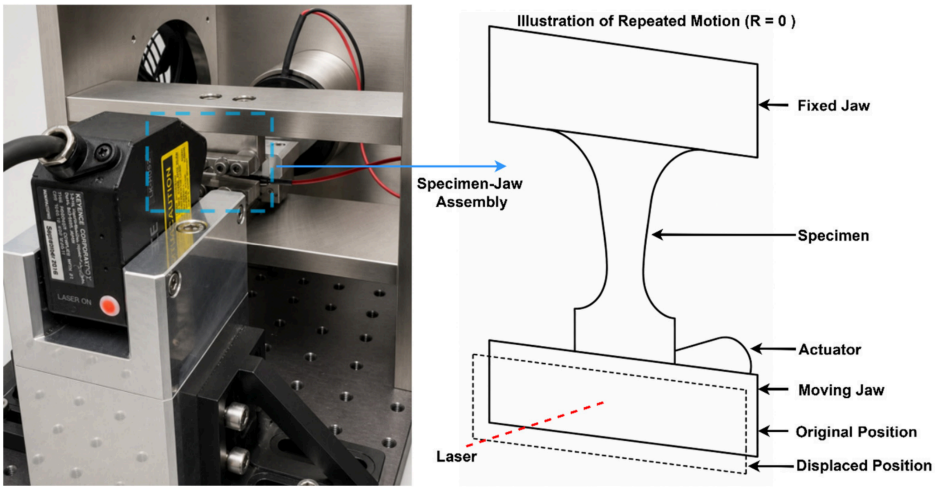


Figure 7. Schematic of fatigue test apparatus.

4.3. Controls and Data Acquisition Procedure

The control of the fatigue tester follows conventional fatigue test control methods. It uses two sensors, a pre-calibrated laser displacement sensor to measure specimen displacement, and a load cell to measure the applied force. The displacement and load signals are processed onboard a Raspberry Pi through an analog-to-digital converter (ADC) with a sampling rate of 860 Hz. A C-based control script provides feedback control, transferring the acquired data via USB to a Windows-based computer, and generates the command signal used to drive the actuator.

For actuator control, the Raspberry Pi generates a square-wave command using the pigpio library in C. This allows for hardware-timed PWM (pulsed width modulation) on Raspberry Pi to ensure an accurate frequency of the resultant square wave. The square wave is then fed into an H-bridge, incorporating a DRV8833 IC, which controls the forward and reverse motion of the shaft by switching the polarity across the actuator. The applied load and corresponding displacement data were continuously recorded using C++ 17 based data acquisition and subsequently processed using MATLAB R2025a.

4.4. Test Method

All tests were conducted at a frequency of 10 Hz and room temperature, using the conventional stress-life (S-N) approach for bending fatigue characterization of the proposed meso-scale specimen geometry. Based on preliminary evaluation of the developed test apparatus, a frequency of 10 Hz provided stable cyclic loading and consistent signal acquisition with minimal measurement noise and was therefore selected for all fatigue experiments. Since the present study primarily focuses on validating the proposed meso-scale specimen design and testing methodology, the potential influence of loading frequency on fatigue behavior was not investigated and will be considered in future work. The temperature of the specimen and components of the test apparatus were monitored using an FLIR infrared thermal camera. and the maximum recorded temperature remained below 30 °C. This indicates that self-heating effects were negligible and that the measured fatigue response was not influenced by thermal degradation.

The experiments were conducted under constant-amplitude, load-controlled conditions with a prescribed stress ratio of $R = 0$, such that the applied load oscillated between a prescribed maximum value, with the zero minimum stress and mean stress corresponding to half of the maximum stress, as illustrated in Figure 8. Although the actuator was driven by a square wave command generated through the H-bridge controller, the measured load and displacement responses exhibited periodic cyclic waveforms rather than an ideal square-wave profile, owing to the noise from dynamic response of the actuator-fixture-specimen system.

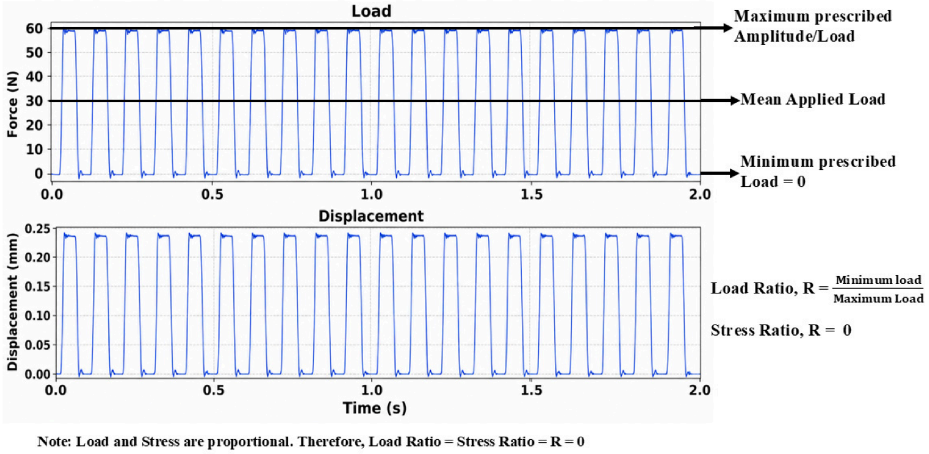


Figure 8. Illustration of loading method for fatigue test at stress ratio, R = 0.

As the primary objective of this study was to verify and quantify the feasibility of proposed specimen design, and the mechanical and fatigue properties of the material were already established (Table 2), a preliminary loading range was first estimated from the analytical stress calculation in conjunction with the known mechanical properties of the material. Based on this estimation, the applied load levels were selected as presented in Appendix A, Table A1 to span the relevant fatigue regime from the near ultimate-strength region toward the endurance-strength region of the S-N curve.

5. Result and Discussion

5.1. Mechanical and Fatigue Properties of 17-4 PH Optimized Geometry

Since the specimen was miniaturized, the actual mechanical properties of 17-4 PH were determined through a mini-tensile testing machine developed by Product Innovation and Engineering LLC (PINE) to find the equivalence with standard data. Subsequently, these basic properties were used for the determination of endurance strength along with

fatigue life-cycle constant (a), fatigue strength exponent (b), surface characteristics and endurance strength correction factors of the optimized specimen by using Equations (7)–(13) and relevant charts and figures from the literature as summarized in Table 2.

5.2. Experimental Validation of Optimized Geometry

The applied load and measured displacement amplitudes remained stable during the test for the majority of fatigue cycles, indicating consistent mechanical behavior within the elastic regime as demonstrated in Figure 9. Then in the plastic regime, as the crack initiated, a gradual increase in displacement amplitude was observed due to the reduction in the structural stiffness [3,67]. Continued crack propagation resulted in a rapid rise in displacement amplitude before complete failure of the specimen (Figure 9). The test was automatically terminated when the displacement monitored and measured by the displacement sensor exceeded the predefined threshold value.

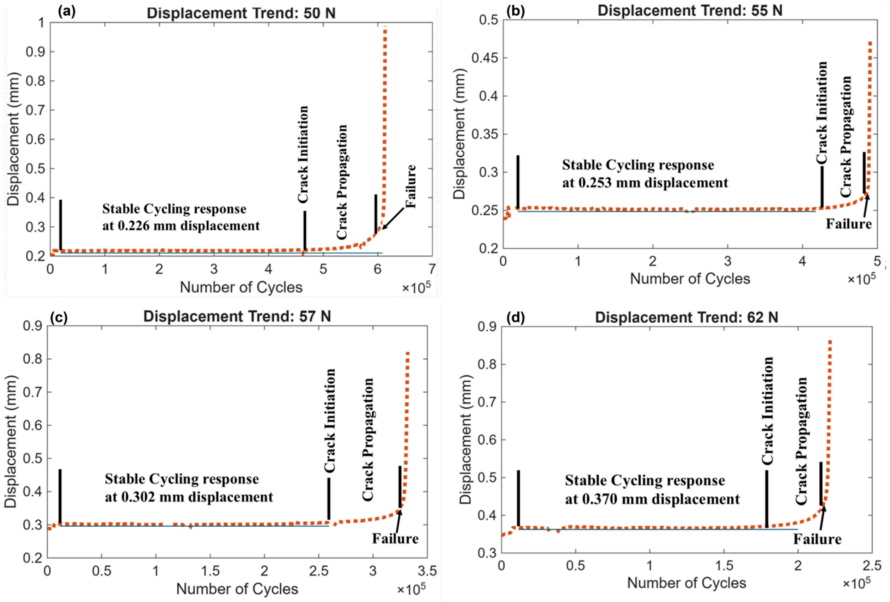


Figure 9. Fatigue behavior of 17-4 PH optimized specimen at different loads: (**a**) 50 N; 0.226mm; (**b**) 55 N; 0.253 mm, (**c**) 57 N; 0.302 mm, and (**d**) 62 N; 0.370 mm.

Figure 10 shows that in all fractured specimens, crack initiation and final fracture occurred at different locations within the gage section. This observation proves the excellent agreement with the finite element prediction of maximum stress distribution across the gage section as presented in Section 3.1. The experimentally observed failure locations confirmed the effectiveness of the geometry optimization process and demonstrated that selected specimen design provides a well-defined fatigue interrogation region. By promoting the crack initiation and propagation within the gage section, the optimized geometry minimizes boundary-induced effects and allows more representative characterization of the material's fatigue behavior. Although the statistical significance of randomness in failure location has not yet been established and remains beyond the scope of the present study, the observed failures occurred within the intended gage region and exhibited variation in crack-initiation locations and propagation directions across the gage. These observations together with uniform stress-distribution support the suitability of the proposed meso-scale specimen for bending fatigue characterization.

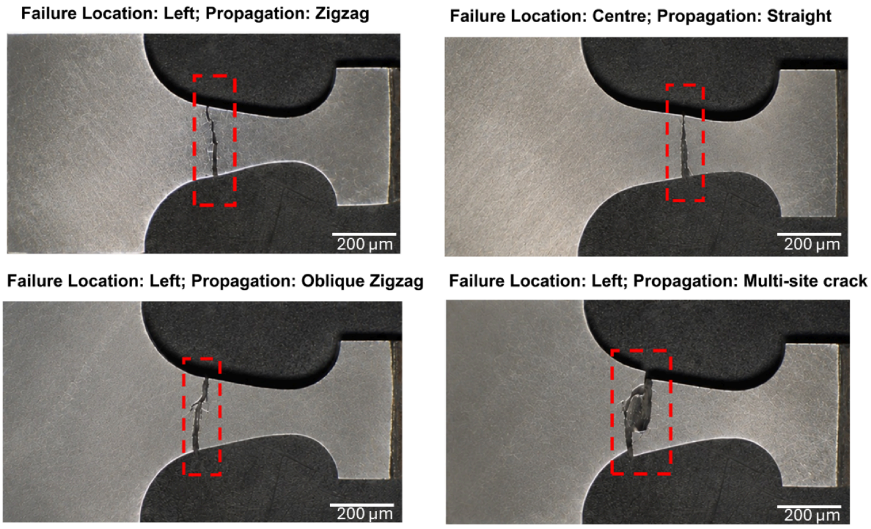


Figure 10. Representative fracture locations and crack-propagation patterns observed within the gage region of the 17-4 PH specimens.

5.3. Experimental Results and Discussion

A total of 24 specimens were tested at different load levels, with selected conditions, including 40, 55, 60, and 65 N, repeated to assess the repeatability of the experimental results, as shown in Figures 11 and 12, and Appendix A, Table A1. In Figure 12, variations in fatigue life were observed among specimens tested at the same load level. Such scatter is expected in fatigue testing and represents specimen-to-specimen variations in microstructure and defect population and associated crack-initiation behavior.

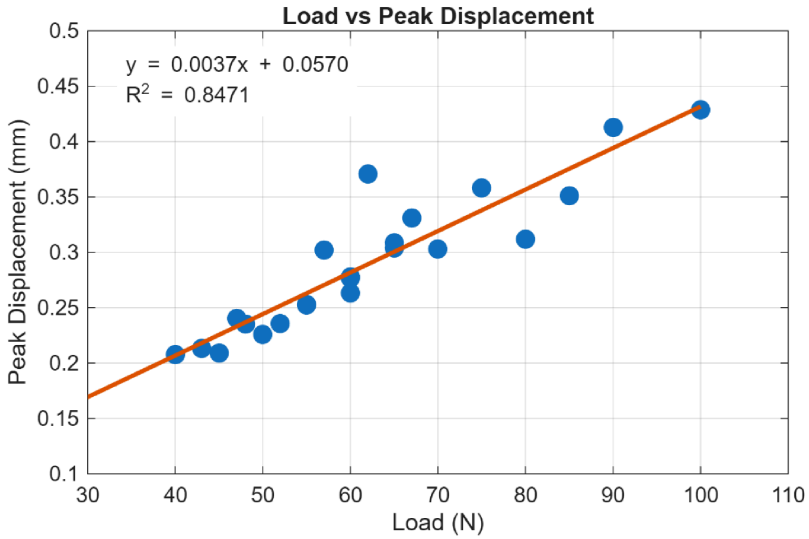


Figure 11. Load vs. peak displacement of 17-4 PH using optimized geometry.

Figures 11 and 12 present the relationships between load versus displacement and load versus number of cycles to failure, respectively. A positive correlation was observed in load-displacement response, such that increasing load resulted in higher peak displacement amplitudes. In contrast, the load-cycle relationship demonstrated the expected inverse trend characteristic of fatigue behavior, where increased load levels caused reduced fatigue life. The fitted curve shows that linear regression relationship yielded coefficients of determination (R^2) of approximately 0.85 for both datasets, indicating good consistency among the experimental measurements.

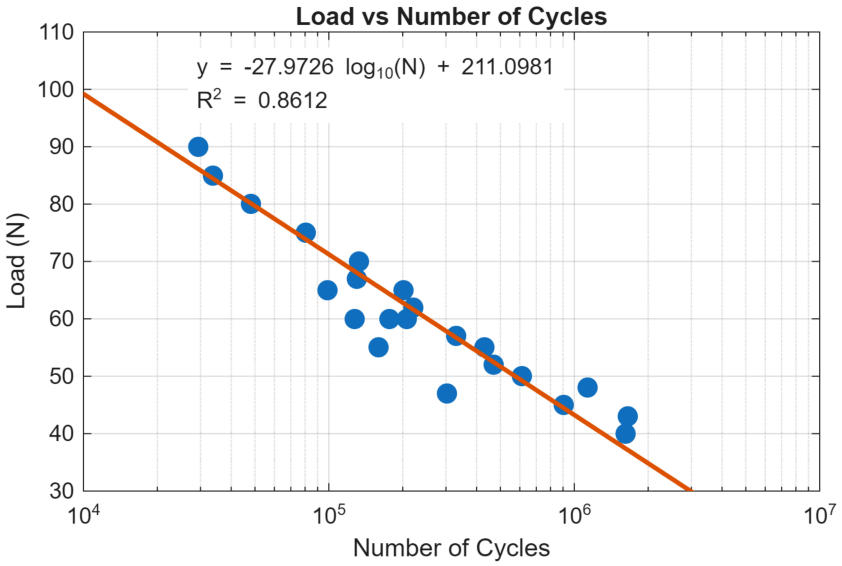


Figure 12. Load vs. number of cycles of 17-4 PH using optimized geometry.

To generate the Wohler S-N curve, the measured peak displacement values were first converted to maximum local bending stress using the stress–displacement relationship given in Equation (15), which was derived by combining Equations (1) and (2). Although, Equation (6) included K_f, in relation to K_t, and q, the optimized specimen geometry exhibited stress-concentration factors approaching unity, as summarized in Figure 4. Therefore, an additional K_f correction factor was not applied in Equation (15). In addition, Equation (1) was derived directly from the actual varying Krouse geometry by incorporating the local bending moment (M), and local section property (I), thereby accounting for geometric variation in the calculation of the maximum local bending stress. Alternating stress (σ_a), and mean stress (σ_m), were then calculated from the maximum bending stress using Equation (16).

$$\sigma_{max} = \frac{E\,B\,\delta}{L_g{}^2} \tag{15}$$

$$\sigma_a = \sigma_m = \frac{\sigma_{max}}{2} \tag{16}$$

Because the fatigue tests were conducted at a stress ratio of ($R = 0$), the calculated maximum stresses were subsequently converted to equivalent fully reversed stresses using Goodman criterion to account for mean stress effect, as explained in section Equivalent Reversible Stress.

Equation (14) was rearranged to obtain Equation (17), in which S_e was replaced by σ_{rev}, and the resulting expression was used to determine equivalent fully reversed stress (σ_{rev}), for each test. These equivalent fully reversed stresses were then treated as effective stress amplitudes and plotted against the corresponding number of cycles to failure for constructing the S-N curve presented in Figure 13, and reported in Appendix A, Table A1. A run-out criterion of 10^6 cycles was adopted such that specimens exceeding this limit without failure were classified as censored run outs and marked with an arrow in the plot. The tests at this endurance limit regime were repeated to verify the observed non-failure behavior, and some tests were extended beyond the initial limit, with the longest run out reaching 2.27×10^6 cycles.

$$\sigma_{rev} = \frac{\sigma_a}{(1 - (\sigma_m / S_{ut}))} \tag{17}$$

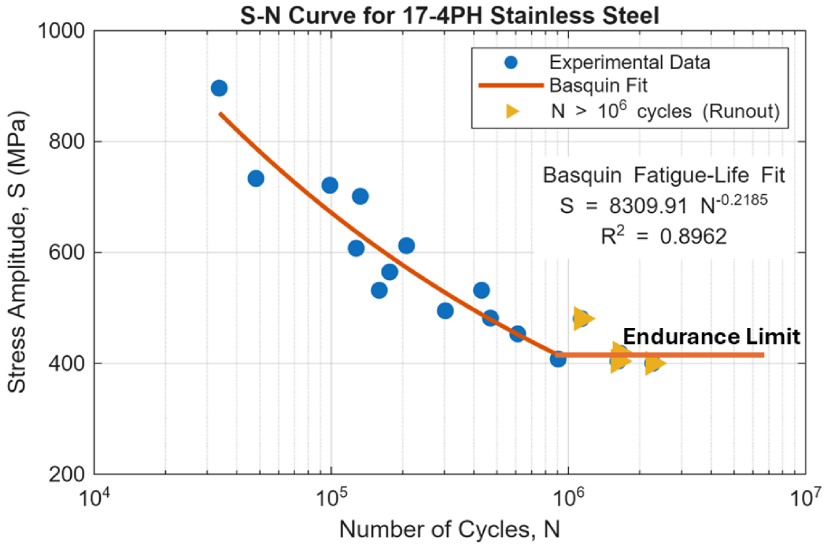


Figure 13. S-N Curve of 174 PH experimented on optimized geometry.

The generated S-N curve exhibits the expected fatigue behavior of metallic materials, with fatigue strength decreasing as the number of cycles to failure increases. Although some scatter is observed in experimental data, the coefficient of determination (R^2) of 0.89 is still comparable with other studies performed on similar Krouse specimens [41] and overall trend remains consistent with conventional fatigue characterization and established theories.

As shown in Figure 14, the experimental results were further compared with the literature on fatigue data studied and reported by Leybold in a technical note of NASA [57]. This standard dataset was widely used to compare the fatigue performance of additively manufactured 17-4 PH steels in multiple studies [68–71]. However, direct quantitative comparison may not be appropriate in this regard due to significant differences in test methods, specimen geometry and size, and the loading mode. For example, the literature fatigue data studied by Leybold on wrought 17-7 PH were obtained from axial fatigue tests of conventionally sized specimens, whereas the present work employed a miniaturized specimen subjected to cyclic bending. Nevertheless, such comparisons provide useful qualitative insight into the performance and reliability of the proposed fatigue characterization approach. The comparison indicates that the literature data exhibited about 27% higher strength than 17-4 PH tested in this study. Several factors may contribute to this difference, including loading mode, stress gradients inherent to bending fatigue, specimen dimensions, surface conditions, and manufacturing-related effects which are the scope of further detailed studies. Despite these differences, both datasets exhibit similar S-N behavior and comparable fatigue-strength degradation trends, proving the validity of the proposed methodology.

Figure 14 also demonstrates a good agreement of this experimental dataset with that of theoretical predictions developed in the present work. Based on the endurance limit at 10^6 cycles, the theoretical model predicted a fatigue strength of about 330 MPa, while the experimentally obtained endurance strength was roughly 400 MPa, representing a difference of nearly 18%. This variation is expected with the reasoning that the theoretical model assumes idealized loading and boundary conditions, whereas the experimental set-up includes clamping effects, load-transfer mechanisms, contact interactions, and other practical factors that influence stress concentrations within the specimen. Moreover, this discrepancy provides a conservative basis for fatigue design. The experimentally observed improved endurance limit manifests that the optimized specimen geometry and testing approach yield a fatigue performance superior to the minimum capability estimated by

the analytical model. This conservative approach is especially advantageous for real-life engineering applications, where underprediction of fatigue strength is generally preferred over overprediction to mitigate the risk of unexpected fatigue failure while in service.

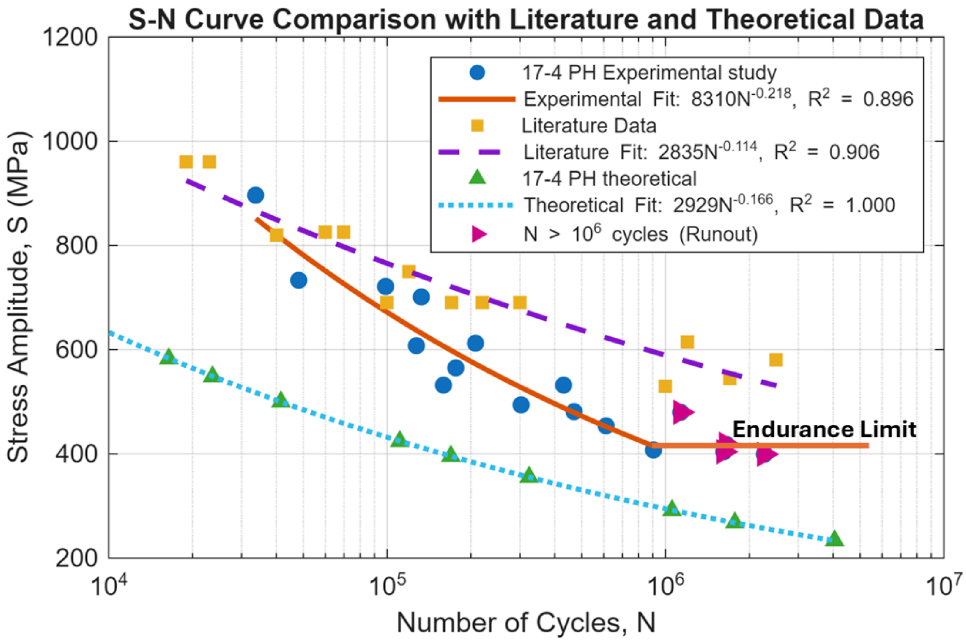


Figure 14. S-N curve comparison with experimental, theoretical, and literature data.

To summarize, the experimental results generally agree with the classic S-N curve and standard method confirming the optimal meso-scale specimen geometry for fatigue behavior. The concordance found between experimental measurements, numerical predictions and published data demonstrates that the proposed specimen geometry is capable of generating representative fatigue life data with substantially lower specimen sizes, material volumes and costs. These results confirm the viability of the improved shape for bending fatigue characterization and suggest the potential for future applicability to high-throughput and high-cycle fatigue testing, and material screening.

6. Conclusions

In this study, a novel meso-scale Krouse-type fatigue specimen and test set-up were successfully developed and validated through a systematic design and optimization strategy, together with the practical experimentation. Specimen geometry was determined through theoretical analysis and subsequently refined using finite element analysis to maximize the effective gage region to ensure a more uniform stress distribution throughout the fatigue interrogation volume. Optimized design successfully moved stress concentration away from the clamping and loading zones and localized fatigue damage within the specified gage section.

The effectiveness of the proposed geometry was verified both by numerical simulations and experimental testing. Finite element analysis justified uniform stress distribution within the gage section, whereas experimental observations confirmed the crack initiation and final fatigue fracture within the optimized region. The experimentally observed failure locations were in good agreement with the numerical predictions, and thus, the geometry optimization methods and accompanying testing methodology were validated.

Furthermore, experimentally determined load-displacement, load-life relationships, and generated S-N curve exhibited consistent trends with conventional fatigue behavior. Comparison with theoretical predictions and literature data further confirmed the ability of

the proposed miniaturized specimen geometry to generate meaningful fatigue-life data. The experimentally determined endurance strength was found to exceed theoretical prediction by approximately 18%, confirming the suitability of the optimized meso-scale fatigue characterization approach to real-life engineering applications. Additionally, from a manufacturing and economic perspective, the elimination of features in conventional specimens, such as holes and notches, contributed to the cost effectiveness of the design by minimizing extra machining complexities and fabrication time. The collective validation techniques and associated observations can adapt the optimized specimen as a practical and scientific solution of fatigue test for application in both research laboratories and manufacturing industries, particularly in additive manufacturing, automobile, aerospace, nuclear and medical sectors, which require rapid and small-scale testing with high fidelity data.

7. Future Works

The feasibility and validation of the developed specimen geometry were evaluated using a single material under a fixed loading frequency, stress ratio, and limited to a single experimental arrangement. Therefore, the authors recommend progressing this research by evaluating the applicability of the proposed specimen geometry across a broader range of materials and manufacturing processes. Further investigations on the influence of loading frequency, surface-induced effects, dimensional tolerances, clamping mechanism, and various loading modes would further strengthen the appropriateness of the suggested methodology. Manufacturing sensitivities, possible edge defects and notch formation in the adjacent features of the geometry during sample preparation need to be justified. The statistical significance for the randomness in failure location along with the repeatability of the fatigue life at each loading condition should be established through further investigation. Finally, comparative studies with conventional fatigue specimens of different shapes and sizes are encouraged to comprehensively evaluate the performance, scalability, and robustness of the proposed meso-scale specimen design alongside establishing correlations between different fatigue characterization approaches for its meaningful adoption and standardization.

Author Contributions: Conceptualization, M.B.U. and S.P.I.; methodology, M.B.U. and T.P.; software, T.P.; experimental validation, M.B.U., S.P.I., T.P. and F.L.; formal analysis, M.B.U. and M.M.P.; investigation, M.B.U. and M.M.P.; resources, F.L.; data curation, M.B.U. and T.P.; writing—original draft preparation, M.B.U.; writing—review and editing, M.B.U., S.P.I., T.P., M.M.P. and F.L.; visualization, M.B.U.; supervision, S.P.I. and F.L.; project administration, F.L. and S.P.I.; funding acquisition, F.L. All authors have read and agreed to the published version of the manuscript.

Funding: This project was funded by the Department of Energy, contract #DE-SC0018879; Kummer I&E (Innovation & Entrepreneurship) Doctoral Fellowship program at Missouri University of Science and Technology, and Product Innovation and Engineering, LLC. The authors express sincere gratitude for their financial support.

Data Availability Statement: The data relevant to the current study is presented in the article. Further inquiries can be directed to the corresponding author.

Conflicts of Interest: Author Mohammad Masud Parvez was employed by the company Articure Inc. The remaining authors declare that the research was conducted in the absence of any commercial or financial relationships that could be construed as potential conflicts of interest.

Appendix A. Data Tables

Table A1. 17-4 PH Stainless Steel Experimental Data of Optimized Geometry.

Specimen	Load_N	Displacement, mm	Thickness, mm	Gage Width, mm	SR, Micron	Stress Amplitude, MPa	No of Cycles, N
1	40	0.19985	0.756	2.508	0.5	387.92	2.27×10^6
2	40	0.20773	0.762	2.468	0.5	412.94	1.62×10^6
3	43	0.21319	0.753	2.492	0.3	420.89	1.65×10^6
4	45	0.20926	0.761	2.503	0.5	416.32	9.06×10^5
5	47	0.24038	0.757	2.486	0.6	501.14	3.02×10^5
6	48	0.23546	0.751	2.475	0.3	481.18	1.13×10^6
7	50	0.22606	0.759	2.519	0.4	461.26	6.12×10^5
8	52	0.23581	0.761	2.522	0.7	491.30	4.70×10^5
9	55	0.25288	0.753	2.475	0.3	535.04	1.59×10^5
10	55	0.25277	0.76	2.472	0.3	541.97	4.30×10^5
11	57	0.30188	0.755	2.495	0.3	703.72	3.31×10^5
12	60	0.26333	0.755	2.497	0.3	570.11	1.77×10^5
13	60	0.27664	0.752	2.599	0.4	610.33	1.28×10^5
14	60	0.2779	0.753	2.523	0.9	615.81	2.08×10^5
15	62	0.37074	0.753	2.585	0.5	996.60	2.20×10^5
16	65	0.30415	0.752	2.535	0.3	707.69	2.02×10^5
17	65	0.30864	0.757	2.556	0.5	732.44	9.87×10^4
18	67	0.33111	0.756	2.502	1.4	821.39	1.30×10^5
19	70	0.30313	0.752	2.594	0.3	703.89	1.32×10^5
20	75	0.35808	0.756	2.525	0.3	942.11	8.04×10^4
21	80	0.31172	0.756	2.472	0.4	742.78	4.82×10^4
22	85	0.35109	0.754	2.483	0.3	905.18	3.37×10^4
23	90	0.41294	0.757	2.449	0.7	1242.54	2.94×10^4
24	100	0.42854	0.759	2.539	0.3	1350.97	3.54×10^4
		Average	0.756	2.511	0.47		

References

1. Norton, R.L. Machine design: An integrated approach. *J. Manuf. Syst.* **1998**, *17*, 236. [CrossRef]
2. Schütz, W. A history of fatigue. *Eng. Fract. Mech.* **1996**, *54*, 263–300. [CrossRef]
3. Ritchie, R.O. Mechanisms of fatigue-crack propagation in ductile and brittle solids. *Int. J. Fract.* **1999**, *100*, 55–83. [CrossRef]
4. Kurotani, Y.; Tanaka, H. Fatigue fracture mechanism of amorphous materials from a density-based coarse-grained model. *Commun. Mater.* **2022**, *3*, 67. [CrossRef]
5. Uddin, M.B.; Isanaka, S.P.; Liou, F. Bending Fatigue in Additively Manufactured Metals: A Review of Current Research and Future Directions. *Crystals* **2025**, *15*, 920. [CrossRef]
6. Lieurade, H.P.; Degallaix, S.; Degallaix, G.; Gauthier, J.P. Fatigue Tests. In *Structural Components: Mechanical Tests and Behavioral Laws*; ISTE: Arlington, VA, USA; John Wiley & Sons: Hoboken, NJ, USA, 2010; pp. 125–192. [CrossRef]
7. *ASTM E468-18*; Standard Practice for Presentation of Constant Amplitude Fatigue Test Results for Metallic Materials. ASTM International: West Conshohocken, PA, USA, 2018. [CrossRef]
8. *ASTM E606-04e1*; Standard Test Method for Strain-Controlled Fatigue Testing. ASTM International: West Conshohocken, PA, USA, 2004. [CrossRef]
9. *ASTM B593-21*; Standard Test Method for Bending Fatigue Testing for Copper-Alloy Spring Materials. ASTM International: West Conshohocken, PA, USA, 2021. [CrossRef]
10. Kulkarni, P.V.; Sawant, P.J.; Kulkarni, V.V. Design and Development of Plane Bending Fatigue Testing Machine for Composite Material. *Mater. Today Proc.* **2018**, *5*, 11563–11568. [CrossRef]

11. Zalnezhad, E.; Sarhan, A.A.D.; Jahanshahi, P. A new fretting fatigue testing machine design, utilizing rotating-bending principle approach. *Int. J. Adv. Manuf. Technol.* **2014**, *70*, 2211–2219. [CrossRef]
12. Vysetti, B. Current Advances in the Miniaturization of Analytical Instruments—Applications in Cosmochemistry, Geochemistry, Exploration, and Environmental Sciences. *Spectroscopy* **2016**, *31*, 40–44.
13. Pagano, C.; Fassi, I. Introduction to Miniaturisation. In *Micro-Manufacturing Technologies and Their Applications*; Springer: Cham, Switzerland, 2017; pp. 1–22. [CrossRef]
14. Bergonzi, L.; Vettori, M.; Moroni, F.; Musiari, F.; Pirondi, A. Experimental validation of miniaturized specimen developed to perform uniaxial tensile test on high performance materials. *IOP Conf. Ser. Mater. Sci. Eng.* **2021**, *1038*, 012070. [CrossRef]
15. Džugan, J.; Rund, M.; Prantl, A.; Konopík, P. Mini-tensile specimen application for sheets characterization. *IOP Conf. Ser. Mater. Sci. Eng.* **2017**, *179*, 012020. [CrossRef]
16. Karnati, S.; Isanaka, S.P.; Zhang, Y.; Liou, F.F.; Schulthess, J.L. A Comparative Study on Representativeness and Stochastic Efficacy of Miniature Tensile Specimen Testing. *Mater. Perform. Charact.* **2022**, *11*, 424–439. [CrossRef]
17. *ASTM E8/E8M-24*; Standard Test Methods for Tension Testing of Metallic Materials. ASTM International: West Conshohocken, PA, USA, 2024. [CrossRef]
18. Hirose, T.; Sakasegawa, H.; Kohyama, A.; Katoh, Y.; Tanigawa, H. Effect of specimen size on fatigue properties of reduced activation ferritic/martensitic steels. *J. Nucl. Mater.* **2000**, *283–287*, 1018–1022. [CrossRef]
19. Sempruch, J.; Tomaszewski, T. Application of mini specimens to high-cycle fatigue tests. *J. Pol. CIMAC* **2011**, *6*, 279–288.
20. Ghadimi, H.; Jirandehi, A.P.; Nemati, S.; Guo, S. Small-sized specimen design with the provision for high-frequency bending-fatigue testing. *Fatigue Fract. Eng. Mater. Struct.* **2021**, *44*, 3517–3537. [CrossRef]
21. Yang, D.; Tang, S.; Hu, Y.; Nikitin, A.; Wang, Q.; Liu, Y.; Li, L.; He, C.; Li, Y.; Xu, B.; et al. A Novel Model of Ultrasonic Fatigue Test in Pure Bending. *Materials* **2022**, *15*, 4864. [CrossRef] [PubMed]
22. Nicoletto, G. Fatigue Behavior of L-PBF Metals: Cost-Effective Characterization via Specimen Miniaturization. *J. Mater. Eng. Perform.* **2021**, *30*, 5227–5234. [CrossRef]
23. Gabel, S.; Merle, B.; Merle, B. Small-scale high-cycle fatigue testing by dynamic microcantilever bending. *MRS Commun.* **2020**, *10*, 332–337. [CrossRef]
24. Hao, W.Q.; Shi, D.Q.; Yang, X.G.; Li, N.N.; Su, S.; Fan, Y.S. Multi-mode fatigue life prediction using machine learning inspired by damage physics. *Int. J. Mech. Sci.* **2025**, *304*, 110723. [CrossRef]
25. Chen, D.; Li, Y.; Liu, K.; Li, Y. A physics-informed neural network approach to fatigue life prediction using small quantity of samples. *Int. J. Fatigue* **2023**, *166*, 107270. [CrossRef]
26. Bao, H.; Wu, S.; Wu, Z.; Kang, G.; Peng, X.; Withers, P.J. A machine-learning fatigue life prediction approach of additively manufactured metals. *Eng. Fract. Mech.* **2021**, *242*, 107508. [CrossRef]
27. Rahman, A.; Ali, M.d.H.; Malik, A.W.; Mahmood, M.A.; Liou, F. Physics-Based Machine Learning Framework for Predicting Structure-Property Relationships in DED-Fabricated Low-Alloy Steels. *Metals* **2025**, *15*, 965. [CrossRef]
28. Kelly, D.A.; Morrison, J.L.M. Effect of specimen size and preparation carbon steel tested in rotating bending and in torsion on the fatigue strength of a plain. *Proc. Inst. Mech. Eng.* **1970**, *185*, 655–664. [CrossRef]
29. Findley, W.N. An Explanation of Size Effect in Fatigue of Metals. *J. Mech. Eng. Sci.* **1972**, *14*, 424–428. [CrossRef]
30. Benedetti, M.; du Plessis, A.; Ritchie, R.O.; Dallago, M.; Razavi, N.; Berto, F. Architected cellular materials: A review on their mechanical properties towards fatigue-tolerant design and fabrication. *Mater. Sci. Eng. R Rep.* **2021**, *44*, 100606. [CrossRef]
31. Sun, C.; Song, Q. A method for predicting the effects of specimen geometry and loading condition on fatigue strength. *Metals* **2018**, *8*, 811. [CrossRef]
32. Tomaszewski, T. Statistical size effect in fatigue properties for mini-specimens. *Materials* **2020**, *13*, 2384. [CrossRef] [PubMed]
33. Yi, M.; Tang, W.; Zhu, Y.; Liang, C.; Tang, Z.; Yin, Y.; He, W.; Sun, S.; Su, S. A holistic review on fatigue properties of additively manufactured metals. *J. Mater. Process. Technol.* **2024**, *329*, 118425. [CrossRef]
34. Tang, R.; Sajuri, Z.; Zhang, P.; Qi, Y.; Zou, Y.; Liu, Z.; Wang, S.; Liu, X. Key factors governing bending fatigue behavior and its evaluation methods in metal additive manufacturing: A review. *Front. Mech. Eng.* **2026**, *12*, 1865030. [CrossRef]
35. Hagnell, M.K.; Khurshid, M.; Åkermo, M.; Barsoum, Z. Design implications and opportunities of considering fatigue strength, manufacturing variations and predictive lcc in welds. *Metals* **2021**, *11*, 1527. [CrossRef]
36. Kaimkuriya, A.; Sethuraman, B.; Gupta, M. Effect of Physical Parameters on Fatigue Life of Materials and Alloys: A Critical Review. *Technologies* **2024**, *12*, 100. [CrossRef]
37. Jimenez-Martinez, M. Manufacturing effects on fatigue strength. *Eng. Fail. Anal.* **2020**, *108*, 104339. [CrossRef]
38. Ganta, M.G.; Kurek, M. Influence of post-processing methods on the fatigue performance of materials produced by selective laser melting (SLM). *Int. J. Adv. Manuf. Technol.* **2025**, *136*, 2003–2034. [CrossRef]
39. Parvez, M.M.; Chen, Y.; Karnati, S.; Coward, C.; Newkirk, J.W.; Liou, F. A displacement controlled fatigue test method for additively manufactured materials. *Appl. Sci.* **2019**, *9*, 3226. [CrossRef]

40. Parvez, M.M.; Pan, T.; Chen, Y.; Karnati, S.; Newkirk, J.W.; Liou, F. High cycle fatigue performance of lpbf 304L stainless steel at nominal and optimized parameters. *Materials* **2020**, *13*, 1591. [CrossRef] [PubMed]
41. Williams, Z.R. Krouse Fatigue for Metals with Elevated Mean Stress. Master's Thesis, Ohio University, Athens, OH, USA, 2020.
42. Haidyrah, A.S.; Newkirk, J.W.; Castaño, C.H. Weibull statistical analysis of Krouse type bending fatigue of nuclear materials. *J. Nucl. Mater.* **2016**, *470*, 244–250. [CrossRef]
43. Saheli, M. Elastic Modulus Determination of Krouse Specimens Through Resonance Using Simple. Master's Thesis, Ohio University, Athens, OH, USA, 2019.
44. Shokrieh, M.M.; Esmkhani, M.; Haghighatkhah, A.R.; Zhao, Z. Flexural fatigue behavior of synthesized graphene/carbon-nanofiber/epoxy hybrid nanocomposites. *Mater. Des.* **2014**, *62*, 401–408. [CrossRef]
45. Ramkumar, A.; Gnanamoorthy, R. Effect of nanoclay addition on the displacement-controlled flexural fatigue behavior of a polymer. *J. Mater. Sci.* **2010**, *45*, 4180–4187. [CrossRef]
46. Ueki, Y. High-speed bending-fatigue testing of composite materials. *IOP Conf. Ser. Mater. Sci. Eng.* **2018**, *388*, 012008. [CrossRef]
47. Gohil, P.; Panchal, H.N.; Sohail, S.M.; Mahant, D.V. Experimental and FEA Prediction of Fatigue Life in Sheet Metal (IS 2062). *Int. J. Appl. Res. Stud.* **2013**, *2*, 1–8.
48. Berchem, K.; Hocking, M.G. A simple plane bending fatigue and corrosion fatigue testing machine. *Meas. Sci. Technol.* **2006**, *7*, N60–N66. [CrossRef]
49. Haidyrah, A.S.; Castaño, C.H.; Newkirk, J.W. An experimental study on bending fatigue test with a krouse-type fatigue specimen. *Trans. Am. Nucl. Soc.* **2014**, *111*, 620–623.
50. Michopoulos, J.G.; Iliopoulos, A.P.; Steuben, J.C.; Kittur, M.; Phan, N.; Salem, A.A.; Satko, D.P.; Karnati, S.; Isanaka, S.P.; Liou, F.W. Multiscale Data Driven Methodology for Accelerating Qualification and Certification of Additively Manufactured Parts. In *Encyclopedia of Materials: Metals and Alloys*; Elsevier: Amsterdam, The Netherlands, 2022; pp. 223–244. [CrossRef]
51. Atlas. *Atlas Quality Management Scope: National Doc: Information Notice Stainless Steel 630 (17-4 PH) Grade Data Sheet Grade 630 (17-4 PH)*; Atlas: Tokyo, Japan, 2021.
52. Rahman, A.; Isanaka, S.P.; Liou, F. A Comprehensive Study of Cooling Rate Effects on Diffusion, Microstructural Evolution, and Characterization of Aluminum Alloys. *Machines* **2025**, *13*, 160. [CrossRef]
53. Williams, A. Structural analysis. In *Theory and Practice*; Butterworth-Heinemann: Oxford, UK, 2009. [CrossRef]
54. Oore, S.; Oore, M. Uniform strength for large deflections of cantilever beams under end point load. *Struct. Multidiscip. Optim.* **2009**, *38*, 499–510. [CrossRef]
55. *ASTM E1823-23*; Standard Terminology Relating to Fatigue and Fracture Testing. ASTM International: West Conshohocken, PA, USA, 2023.
56. Kuhn, P.; Langley, H.F.H. *An Engineering Method for Estimating Notch-Size Effect in Fatigue Tests on Steel*; National Advisory Committee for Aeronautics: Washington, DC, USA, 1952.
57. Leybold, H.A. *Axial-Load Fatigue Tests on 17-7 PH Stainless Steel Under Constant-Amplitude Loading*; NASA: Washington, DC, USA, 1960.
58. Young, W.C.; Budynas, R.G. *Roark's Formulas for Stress and Strain*; McGraw-Hill: Columbus, OH, USA, 2002.
59. Budynas, R.G.; Nisbett, J.K. Charts of Theoretical Stress-Concentration Factors K * t. In *Shigley's Mechanical Engineering Design*; McGraw-Hill: New York, NY, USA, 2011.
60. Tipton, S.M.; Sorem, J.R.; Rolovic, R.D. Updated Stress Concentration Factors for Filleted Shafts in Bending and Tension. *J. Mech. Des.* **1996**, *118*, 321–327. [CrossRef]
61. Shigley, J.E.; Mischke, C.R.; Brown, T.H. *Standard Handbook of Machine Design*; McGraw-Hill: Washington, DC, USA, 1996.
62. Budynas, R.G.; Nisbett, J.K.; Shigley, J.E. *Shigley's Mechanical Engineering Design*; McGraw-Hill: New York, NY, USA, 2011.
63. Juvinall, R.C.; Marshek, K.M. *Fundamentals of Machine Component Design*; John Wiley & Sons: Hoboken, NJ, USA, 2019.
64. Khan, A.A.; Ali, M.B.M.; Shaffiar, N.B.M. Relationship of Surface Roughness with Current and Voltage During Wire EDM. *J. Appl. Sci.* **2006**, *6*, 2317–2320. [CrossRef]
65. Parvez, M.M.; Patel, S.; Isanaka, S.P.; Liou, F. A novel laser-aided machining and polishing process for additive manufacturing materials with multiple endmill emulating scan patterns. *Appl. Sci.* **2021**, *11*, 9428. [CrossRef]
66. Lu, H.; Wang, D.; Wu, S.; Pan, Z.; Wang, G.; Guo, G.; Tian, Y.; Xiang, D. A review of laser polishing on Ti6Al4V based on energy density. *J. Mater. Process. Technol.* **2024**, *331*, 118520. [CrossRef]
67. Zhao, X.; Su, S.; Wang, W.; Zhang, X. Metal magnetic memory inspection of Q345B steel beam in four point bending fatigue test. *J. Magn. Magn. Mater.* **2020**, *514*, 167155. [CrossRef]
68. Concli, F.; Bonaiti, L.; Gerosa, R.; Cortese, L.; Nalli, F.; Rosa, F.; Gorla, C. Bending fatigue behavior of 17-4 PH gears produced by additive manufacturing. *Appl. Sci.* **2021**, *11*, 3019. [CrossRef]
69. Yadollahi, A.; Shamsaei, N.; Thompson, S.M.; Elwany, A.; Bian, L.; Mahmoudi, M. Fatigue behavior of selective laser melted 17-4 PH stainless steel. *Int. J. Fatigue* **2017**, *94*, 218–235. [CrossRef]

70. Maccioni, L.; Fraccaroli, L.; Borgianni, Y.; Concli, F. High-Cycle-Fatigue Characterization of an Additive Manufacturing 17-4 PH Stainless Steel. *Key Eng. Mater.* **2021**, *877*, 49–54. [CrossRef]
71. Scott-Emuakpor, O.; Schwartz, J.; George, T.; Holycross, C.; Cross, C.; Slater, J. Bending fatigue life characterisation of direct metal laser sintering nickel alloy 718. *Fatigue Fract. Eng. Mater. Struct.* **2015**, *38*, 1105–1117. [CrossRef]

Disclaimer/Publisher's Note: The statements, opinions and data contained in all publications are solely those of the individual author(s) and contributor(s) and not of MDPI and/or the editor(s). MDPI and/or the editor(s) disclaim responsibility for any injury to people or property resulting from any ideas, methods, instructions or products referred to in the content.